Computation of Vectoring Nozzle Performance

Patrick L. Cheatham,* Steven H. Walker,† and Marvin C. Gridley†
Wright Research and Development Center, Wright-Patterson Air Force Base, Ohio 45433

As an initial step toward greater application of computational fluid dynamics to airframe/exhaust nozzle integration efforts, Euler codes were applied to numerically evaluate the internal performance of three advanced thrust vectoring nozzles developed for aircraft control. Nozzle geometry parameters included: pitch and yaw vector angles, sidewall length, sidewall deflection, and thrust reverser position. Computed pressure distributions and nozzle thrust and vectoring performance were compared to experimental data; agreement was excellent for vectoring configurations, and marginal for a reversing configuration.

Nomenclature

A = cross-sectional area, cm^2
C_{fg} = nozzle gross thrust coefficient, F_g/F_i
F_g = nozzle gross thrust, kN
F_i = nozzle ideal isentropically expanded thrust, kN
NPR = nozzle pressure ratio, P_{t8}/P_0
P_s = static pressure, kPa
P_t = total pressure, kPa
SC = sidewall containment, percentage of divergent flap length
δ_p = hardware pitch vector angle, deg
δ_{pe} = effective pitch vector angle, deg
δ_r = hardware thrust reverse angle, deg
δ_{ye} = effective yaw vector angle, deg
Θ_s = sidewall deflection angle, deg
Θ_{yf} = yaw flap deflection angle, measured from the divergent flap plane, deg

Subscripts

0 = freestream conditions
7 = nozzle entrance (afterburner or turbine exit) conditions
8 = nozzle hardware throat conditions
9 = nozzle exit (divergent flap trailing edges) conditions

Introduction

IN recent years, hardware and software have progressed to improve the application of computational fluid dynamics (CFD) to design and evaluation tasks in aerodynamics. This article describes the results to date of a successful effort to utilize available CFD techniques to design and evaluate aircraft/exhaust nozzle integrations. Included herein are the results of an initial emphasis to evaluate nozzle internal performance using inviscid numerical flow solvers. The method was tested, refined, and validated for several advanced exhaust nozzles, each having a significant experimental data base.

Background

Future tactical military aircraft designed for high performance will require integration of advanced thrust vectoring and reversing (TV/TR) nozzles for enhanced control, maneuverability, and safety. The effectiveness of such nozzles is primarily measured in thrust efficiency and achievable thrust vector angles, which are functions of nozzle internal aerodynamic performance. Therefore, an important goal of exhaust nozzle integration research is to understand the internal aerodynamic performance of advanced exhaust nozzles, allowing comparative evaluation of nozzle types, as well as optimization of individual nozzle designs. A recently completed experimental study of numerous advanced vectoring exhaust nozzle concepts brought to attention large discrepancies between expected and measured internal performance.[1] Computational methods offer a means of bridging the gap between conceptual design and detailed experimental test.

Objective

Ultimately, a comprehensive CFD capability to evaluate aircraft/exhaust nozzle integration performance is desired. A key milestone toward achievement of this overall goal is to establish a capability to evaluate exhaust nozzle internal performance. Following initial design and empirical analysis, this capability will provide relatively inexpensive and rapid preliminary design evaluation, guiding and complementing more detailed experimental test and evaluation. Two additional objectives are to improve the efficiency of the computational process and to gain specific experience applying CFD to airframe/exhaust nozzle integration flow studies.

Approach

Algorithms that solve the inviscid flow equations were used to numerically generate internal performance data for three advanced exhaust nozzle designs. Several different advanced thrust vectoring methods and one thrust reversing method were represented by the three nozzles. Each design was chosen for CFD evaluation based on its applicability to contemporary exhaust nozzle research and its experimental data base.

Inviscid analyses were used throughout, as viscous effects encountered in expanding internal flow are limited. Typically, three-dimensional geometry models were required to adequately represent the nozzle configurations; however, a thrust reversing configuration was modeled two-dimensionally, and several pitch vectoring configurations were modeled in both two and three dimensions. An unstructured grid generator and flow solver were used on the complex two-dimensional reverser configuration, whereas a structured grid generator and flow solver were used on all other configurations. Numerically generated data were reduced and compared to corresponding experimental data, establishing the accuracy of the method.

Presented as Paper 90-2752 at the AIAA/SAE/ASME/ASEE 26th Joint Propulsion Conference, Orlando, FL, July 16–18, 1990; received Aug. 16, 1990; revision received Nov. 21, 1990; accepted for publication Nov. 21, 1990.

*Airframe-Propulsion Integration Engineer, Flight Dynamics Laboratory; First Lieutenant, U.S. Air Force.

†Airframe-Propulsion Integration Engineer, Flight Dynamics Laboratory. Member AIAA.

Description of Methods

In general, all of the nozzles were evaluated in the same manner. For each configuration to be evaluated, a suitable grid was generated and a flow solver was run on the grid until a converged solution was achieved. The flow solution step was repeated for each NPR of interest. Finally, for each solution, numerically generated data were reduced by direct extraction of flow quantities along surfaces of interest, and by pressure area integrations to obtain nozzle performance parameters.

Grid Generation

Structured geometry grids were created using several codes. The I3G/VIRGO code was used to create structured two-dimensional grids and geometry data bases for three-dimensional grids.[2] The GRIDGEN series of codes was used to generate faces of three-dimensional multiblock grids.[3] An in-house code was then used to fill and smooth these three-dimensional grids. Two-dimensional unstructured grids were created by an in-house code, which uses Delaunay triangulation to create grid cells in a triangular mesh.[4]

All the above codes were run interactively on graphics workstations, except the three-dimensional grid generation code, which was run in batch mode on a supercomputer.

Flow Solution

Flow solutions for structured geometry grids were determined by the in-house MERCURY code, which is based on Euler's inviscid equations of motion and uses Jameson's finite-volume cell-centered algorithm.[5] Further details concerning this solver can be found in Ref. 6. This code was run on a supercomputer.

Flow solutions for two-dimensional unstructured grids were determined by an Euler code that uses an algorithm based on Collela's second-order Riemann solver.[7,8] This code was run on a supercomputer as well as on graphics workstations.

Data Reduction

Computed pressures were extracted from the flow solutions along internal surface traces aligned with experimental pressure tap locations. Computed pressures were interpolated where geometry grid coordinates did not exactly correspond to the traces of pressure tap coordinates.

For all three-dimensional solutions, computed thrust performance was determined by pressure area integrations along interior nozzle walls and momentum flux integrations across control surfaces. The total thrust determined from these integrations was used as a measure of nozzle gross thrust F_g. For inviscid flow computations, this value does not account for mass flow leakage or viscous boundary-layer effects. However, both effects should be small for internal nozzle flow, and should be insignificant in the corresponding experimental data. Ideal isentropically expanded thrust F_i was calculated based on the computed total mass flow entering the nozzle. Effective thrust vector angles δ_{pe} and δ_{ye} were evaluated by taking ratios of F_g components, and nozzle gross thrust coefficient C_{fg} was evaluated by taking the ratio of computed F_g to computed F_i.

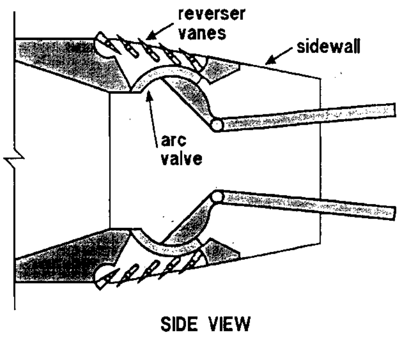

Fig. 1 F-15 S/MTD nozzle design.

Nozzle Designs

F-15 S/MTD Two-Dimensional TV/TR Nozzle

The nozzle installed on the F-15B Short Takeoff and Landing/Maneuver Technology Demonstrator (S/MTD) is a two-dimensional (rectangular cross-section) nozzle featuring pitch vectoring and thrust reversing.[9]

The nozzle design is depicted in Fig. 1. A circular to rectangular transition section lies between the engine and the two-dimensional nozzle. Aft of the transition, valves at top and bottom control the amount of exhaust released to the thrust reversers. Reverse thrust angle δ_r is controlled by parallel airfoil-shaped vanes beyond each control valve. These vanes vary in position angle from 5 to 140 deg, referenced from the negative aircraft longitudinal axis. Angles between 5 and 90 deg produce thrust spoiling, whereas angles between 90 and 140 deg produce thrust reversing. Aft of the reversers, upper and lower divergent flaps are hinged to the convergent flaps at the hardware throat, controlling area ratio (A_9/A_8) and hardware pitch vector angle δ_p. When in full-thrust reverse mode, the upper and lower hinges meet to feed all exhaust to the reversers. The nozzle is designed for δ_p between -20 and 20 deg, and features approximately 60% SC beyond the hardware throat.[10]

A 25% scale model of the F-15 S/MTD nozzle was statically tested in 1985. The cold test provided internal aerodynamic data for the nozzle operating in conventional mode, reverse mode, and in the transition mode between conventional and reverse. Force balance data was not acquired during this test.[10]

Three-Hinge Two-Dimensional TV Nozzle

The three-hinge nozzle is a two-dimensional nozzle featuring both pitch and yaw vectoring.

The nozzle design, depicted in Fig. 2, uses divergent flap deflections to control area ratio and hardware pitch vector angle. Effective yaw vector angle δ_{ye} is primarily controlled by deflectable yaw flaps hinged on each divergent flap. The sidewalls can also be deflected to open a less confining path for yaw vectored flow. The amount of effective yaw vectoring is thus controlled by the combined effects of yaw flap deflection angle (Θ_{yf}: 0 deg when stowed and 90 deg when perpendicular to divergent flap), sidewall deflection angle Θ_s, and SC.[1]

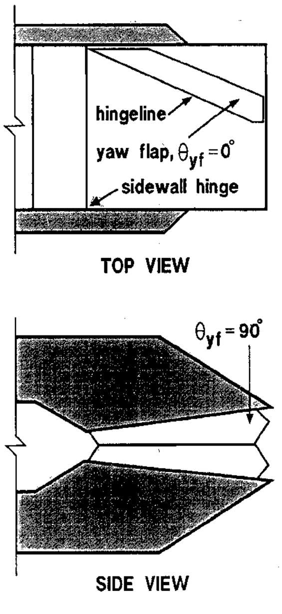

Fig. 2 Three-hinge nozzle design.

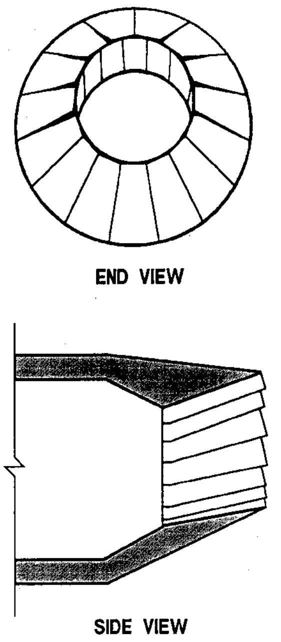

Fig. 3 Balanced beam nozzle design.

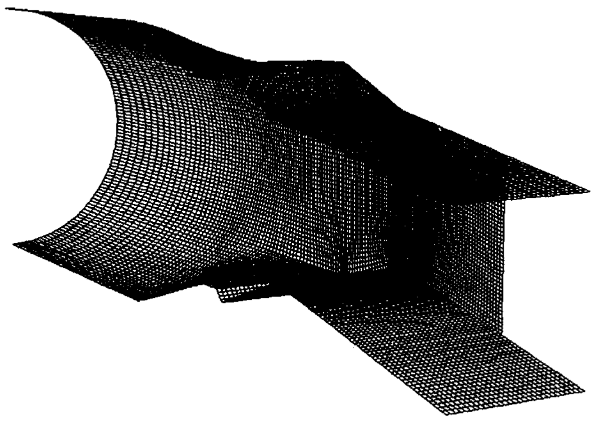

Fig. 4 Three-dimensional internal surface grid; F-15 S/MTD nozzle in conventional mode: $\delta_p = 10$ deg.

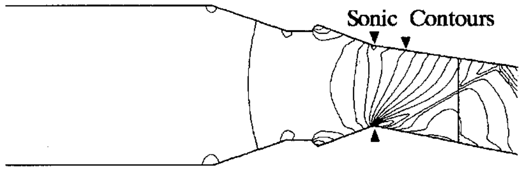

Fig. 5 Centerline profile Mach number contours; F-15 S/MTD nozzle in conventional mode: $\delta_p = 10$ deg, NPR = 5.43.

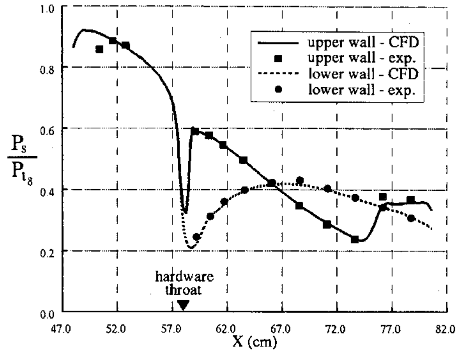

Fig. 6 Centerline pressure ratio comparison; F-15 S/MTD nozzle in conventional mode: $\delta_p = 5$ deg, NPR = 5.25.

A 12% scale model of the three-hinge design was statically tested in 1988. The cold test provided force balance data, along with limited internal aerodynamic data, for pure pitch vector, pure yaw vector, and combined vector modes.[1]

Balanced Beam Axisymmetric TV Nozzle

The balanced beam nozzle is designed for axisymmetric pitch and yaw vectoring.

The nozzle design is depicted in Fig. 3. Area ratio and thrust vectoring (in any plane) are controlled by synchronized deflection of the overlapping divergent flaps.[11]

A subscale model of the balanced beam nozzle was statically tested in 1989, providing internal aerodynamic and force balance data.[11]

Results

F-15 S/MTD Two-Dimensional TV/TR Nozzle

Conventional Mode

Three conventional mode geometries were evaluated, each representing the nozzle configured with a hardware throat area (A_8) of 45 in.^{2} and an exit-to-throat area ratio (A_9/A_8) of 1.1. The design NPR for this area ratio is 3.05. The three geometries featured hardware pitch vector angles (δ_p) of 0, 5, and 10 deg. For each vector angle, NPR values in the experimental test data nearest to 3.0 and 5.0 were chosen as CFD solution NPRs. Both two- and three-dimensional structured grids were created for each of the geometries. Two-dimensional solutions did not reproduce three-dimensional flow behavior beyond nozzle sidewall trailing edges but were accomplished to assess their speed and centerline accuracy vs full three-dimensional solutions.

Figure 4 shows three-dimensional grid surfaces corresponding to internal hardware of the S/MTD nozzle pitch vectored downward at $\delta_p = 10$ deg. Only the right half of the nozzle was modeled, as the left and right halves are mirror reflections.

Figure 5 presents the computed flow behavior through the S/MTD nozzle for this grid at NPR = 5.43. A side profile of Mach number is presented at the nozzle's symmetry plane, with contours generally increasing in magnitude from left to right in 0.1 increments. Sidewall trailing edge location is indicated by a vertical line.

With downward vectoring, the sonic throat stays anchored at the lower hardware throat corner, but rotates aft along the upper divergent flap. A surface connecting these two locations corresponds to the minimum cross-sectional area of the nozzle. At both the upper and lower hardware throat corners (or convergent-divergent flap hinges), nearby flow accelerates in response to the sharpness of the corners. Locally, this expansion is stronger than that warranted by the nozzle expansion area ratio (A_9/A_8). Therefore, a small normal shock sits downstream of the upper hardware throat corner, and a weak oblique shock originates downstream of the lower corner.

With few exceptions, comparisons of three-dimensional CFD data to experimental data are excellent throughout the nozzle. Flow solution pressure distributions, such as those shown in Fig. 6, closely match experimental pressure values at upper and lower divergent flap centerlines and sidelines (pressures just inside from the sidewall). However, when vectoring downward, the lower divergent flap computed results show pressure discrepancies between 4 and 8% just downstream of the lower hardware throat corner. At this location, computed pressures are slightly lower than experimental pressures. A likely explanation for this difference is that the inviscid flow solver, unable to model any flow path smoothing due to viscous effects, produces an expansion around the corner that is stronger than in reality. Additionally, pressures do not match well at the reverser valve-convergent flap juncture, where the experimental test report suggests a recirculation eddy.[10] This eddy is not evident from the inviscid flow solver data and is likely due to viscous separation.

Flow solutions on two-dimensional grids rapidly produced data effectively identical to the three-dimensional solution data along the nozzle's symmetry plane. However, as expected, flow in regions off centerline and downstream of the sidewall was poorly represented by the two-dimensional solutions.

Figure 7 presents an example of thrust performance determined from the three-dimensional flow solutions. Computed effective pitch vector angle δ_{pe} is compared to hardware pitch vector angle δ_p. No experimental force balance data is available for this nozzle. At NPRs near 2.7, which represents slightly overexpanded flow, effective vector angles essentially match hardware vector angles for all vector geometries. However, at NPRs near 5.0, which represents significantly underexpanded flow, effective vector angles are about 25% less than hardware angles. This suggests substantial flow turning losses, likely due to shock structures in the divergent section.

Reverse Mode

The reverse mode geometry represents the nozzle with the conventional flow path completely closed and the reverser fully open. Reverser vanes are set to $\delta_r = 135$ deg. A flow solution was obtained at NPR = 2.71 using a two-dimensional unstructured grid. Figure 8 shows the triangular mesh grid of the reverser geometry. The grid was created for the top half of the nozzle, as the top and bottom halves are mirror reflections.

Figure 9 illustrates the computed flow behavior through the reverser region. Flow rapidly accelerates and then decelerates as it rounds the elbow corner between the transition section and the open reverser valve. In addition, velocity vectors (not shown) suggest recirculation eddies in stagnant flow regions on either side of the reverse flow path.

Pressures were compared at 20 tap locations within the reverser. Data agree very well at seven tap locations along the closed convergent flap (the nearly vertical surface in Fig. 8). Along this flap, computed pressures differ a maximum of 1.6% from experimental values. However, computed pressures are, on the average, 15% greater than experimental values for seven tap locations on the surfaces downstream of (or above) the elbow turn. Additionally, computed pressures average 19% lower than experimental values for six locations between the reverser vanes. These discrepancies show that the inviscid solver was unable to properly reproduce such a flowfield.

Three-Hinge Two-Dimensional TV Nozzle

Three pure yaw vector geometries were evaluated, each representing the nozzle configured with a hardware throat area (A_8) of 3.5 in.^{2} and an exit-to-throat area ratio (A_9/A_8) of 1.8. The design NPR for this area ratio is 8.8. All three geometries featured no pitch vectoring and fully deflected right yaw flaps ($\Theta_{yf} = 90$ deg). The geometries differed in SC and sidewall deflection angle Θ_s. Two geometries featured undeflected sidewalls ($\Theta_s = 0$ deg), each with a different amount of SC (70 and 55%). The third geometry featured a deflected long sidewall ($\Theta_s = 25$ deg and SC = 70%). For each configuration, flow solutions were obtained at NPR values near 6.0. A single three-dimensional structured grid was created, on which variations of flow solver boundary conditions enabled modeling of each of the three geometries.

Figure 10 shows three-dimensional grid surfaces corresponding to internal hardware of the three-hinge nozzle yaw

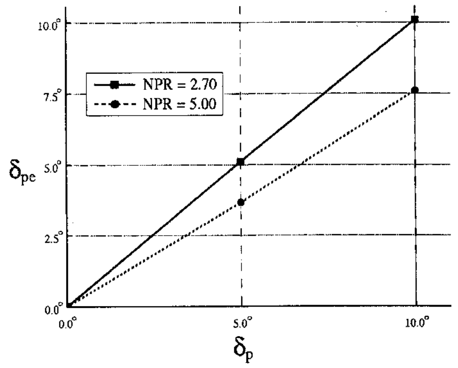

Fig. 7 Comparison of computed effective pitch vector angle to hardware pitch vector angle; F-15 S/MTD nozzle in conventional mode.

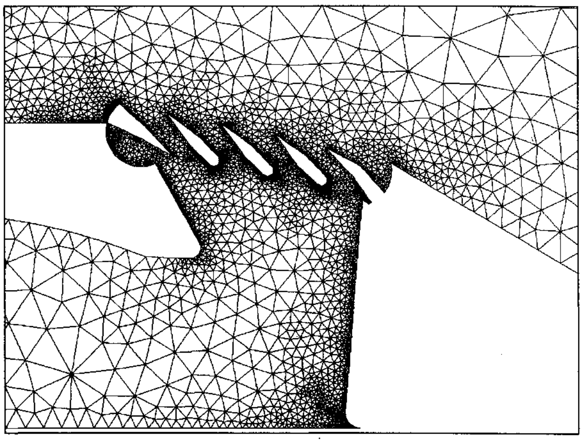

Fig. 8 Two-dimensional unstructured grid; F-15 S/MTD nozzle in reverse mode: $\delta_r = 135$ deg.

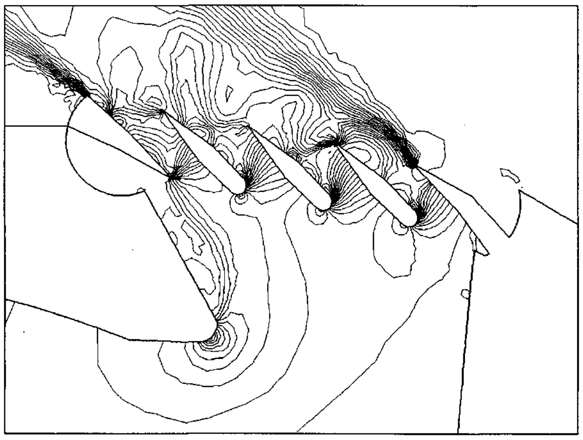

Fig. 9 Mach number contours; F-15 S/MTD nozzle in reverse mode: $\delta_r = 135$ deg, NPR = 2.71.

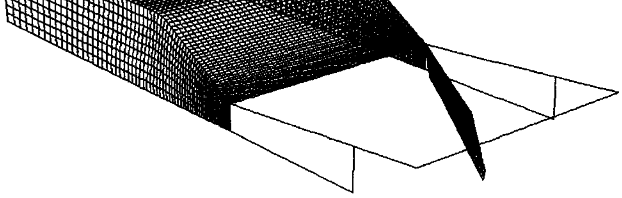

Fig. 10 Three-dimensional internal surface grid with yaw deflector emphasized; three-hinge nozzle: $\delta_p = 0$ deg, $\Theta_{yf} = 90$ deg, $\Theta_s = 0$ deg, SC = 70%.

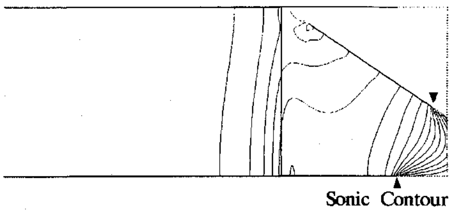

Fig. 11 Centerline top view Mach number contours; three-hinge-nozzle: δ_p = 0 deg, Θ_{yf} = 90 deg, Θ_s = 0 deg, SC = 70%, NPR = 6.0.

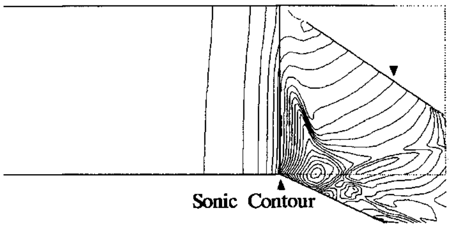

Fig. 12 Centerline top view Mach number contours; three-hinge nozzle: δ_p = 0 deg, Θ_{yf} = 90 deg, Θ_s = 25 deg, SC = 70%, NPR = 5.6.

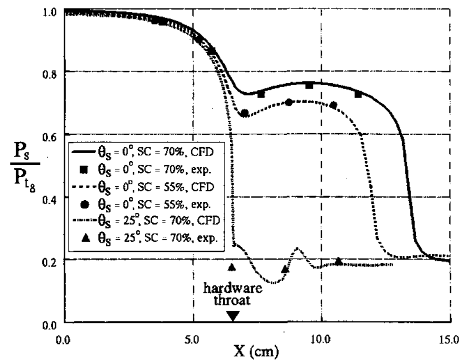

Fig. 13 Left sidewall centerline pressure ratio comparison; three-hinge nozzle: δ_p = 0 deg, Θ_{yf} = 90 deg, NPR ≅ 6.0.

vectored with Θ_{yf} = 90 deg, Θ_s = 0 deg, and SC = 70%. Only the upper half of the nozzle is shown, due to symmetry between the upper and lower halves. The upper divergent flap and the upper half of each sidewall are shown in outline only. The yaw deflector leading edge is located near the far wall at the beginning of the divergent section. The deflector extends left and aft, toward the viewer.

Figures 11 and 12 illustrate examples of computed flow behavior through the yaw vectored three-hinge nozzle. Figure 11 was created from a solution at NPR = 6.0 of the Θ_s = 0 deg, SC = 70% geometry. Figure 12 was created from a solution at NPR = 5.6 of the Θ_s = 25 deg, SC = 70% geometry. Top views of Mach number contours are presented at the symmetry plane.

The undeflected sidewall causes the nozzle to behave as a convergent nozzle rather than a convergent-divergent nozzle. In contrast, the 25-deg deflected sidewall allows the nozzle to maintain convergent-divergent characteristics, but creates a very complex flowfield with convoluted shock structures dominating the flow on the left side of the nozzle (looking upstream).

Pressure comparisons along left sidewall centerlines are presented in Fig. 13. Data are presented for all three configurations. Computed and measured pressures match well, with an exception at the hardware throat tap for the deflected sidewall geometry. Pressure distributions show that both the 55 and 70% containment undeflected sidewall configurations produce convergent nozzle flow behavior. However, the 55% sidewall allows the sonic throat to move further upstream.

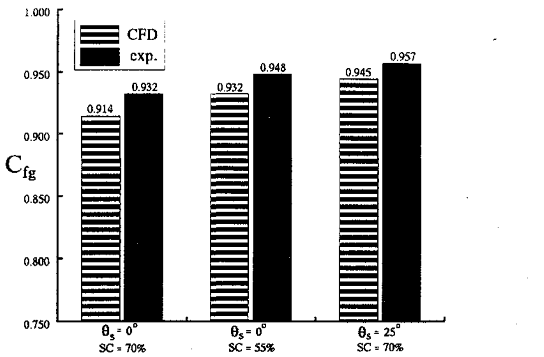

Fig. 14 Gross thrust coefficient comparison; three-hinge nozzle: δ_p = 0 deg, Θ_{yf} = 90 deg, NPR ≅ 6.0.

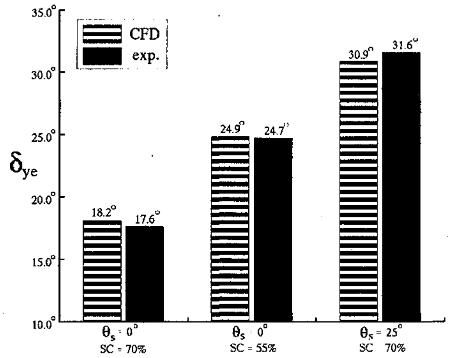

Fig. 15 Effective yaw vector angle comparision; three-hinge nozzle: δ_p = 0 deg, Θ_{yf} = 90 deg, NPR ≅ 6.0.

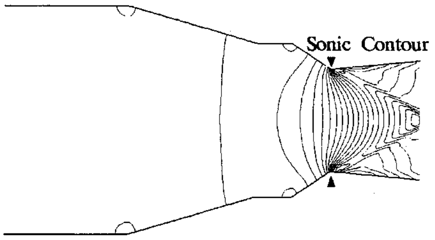

Fig. 16 Centerline profile Mach contours; balanced beam nozzle: δ_p = 10 deg, short divergent flap, NPR = 5.0

Computed values of gross thrust coefficient C_{fg} and effective yaw vector angle δ_{ye} are compared to experimental values in Figs. 14 and 15. Gross thrust F_g is not presented due to dissimilar solution NPR values; however, for the three configurations, discrepancies between computed and measured F_g range from 1.4 to 4.2%.

Both computed and measured C_{fg} and δ_{ye} values indicate that the undeflected sidewall yaw vectored nozzle becomes more efficient as sidewall containment is decreased. Nozzle efficiency is further improved by deflection of the sidewall, greatly increasing the freedom of the flow to escape laterally. Discrepancies between computed and measured δ_{ye} are surprisingly small, whereas those between computed and measured C_{fg} are nearer the magnitude of the F_g discrepancies previously mentioned.

Balanced Beam Axiymmetric TV Nozzle

Three geometries were evaluated, each representing the nozzle configured with a hardware throat area (A_8) of 4.03 in.^{2}

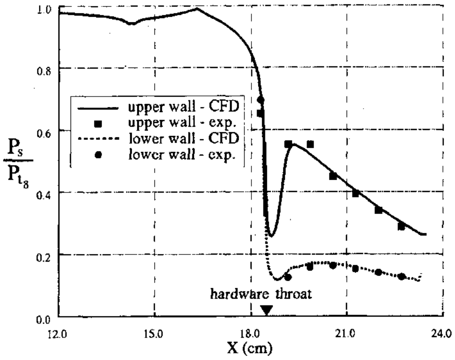

Fig. 17 Pressure ratio comparison; balanced beam nozzle: $\delta_p = 10$ deg, short divergent flap, NPR = 5.0.

and an exit-to-throat area ratio (A_9/A_8) of 1.35. The solution NPR for each geometry was 5.0, which is the design NPR for this area ratio. Two of the geometries featured short divergent flaps, one with $\delta_p = 0$ deg and the other with $\delta_p = 10$ deg. (The symbol δ_p is used for convenience, assuming that the multiaxis vector acts only in the pitch plane.) The third geometry featured long flaps with $\delta_p = 0$ deg. A separate three-dimensional structured grid was created for each geometry.

Figure 16 presents the computed flow behavior through the unvectored balanced beam nozzle with short flaps. Mach number contours are presented at a symmetry plane. An oblique shock cone originates just downstream of the hardware throat, in an axisymmetric equivalent of the behavior noted for the S/MTD and three-hinge nozzles. Just as for the two-dimensional nozzles, this is due to the sharpness of the turn at the hardware throat corner and the corresponding local overexpansion.

Flow solution pressure distributions for the short flap $\delta_p = 10$ deg configuration are compared to measured values in Fig. 17, which presents data through the convergent and divergent sections on the upper and lower wall segments.

For the three configurations, computed values of gross thrust coefficient C_{fg} differ from measured values a maximum of 0.4%, the computed value consistently being slightly greater than the measured value. Effective pitch vector angle δ_{pe} for the 10-deg vectored case also compares well; the computed value is 13.33 deg, 1.3% below the measured value of 13.51 deg. Both values are greater than expected for this hardware vector angle.

Conclusions

Internal performance of three advanced exhaust nozzles for aircraft control was evaluated using Euler algorithm numerical solutions. Two-dimensional and axisymmetric nozzle designs were evaluated, and the advanced nozzle features of pitch vectoring, yaw vectoring, and thrust reversing were investigated. Computed static pressure data were compared to experiment for all three nozzles, and thrust and vectoring performance were compared to experiment for two of the three nozzles.

For thrust vectoring nozzle configurations, three-dimensional inviscid flow solutions generally provided excellent predictions of nozzle internal flow, including thrust, vectoring performance, and pressure distributions. These predictions remained accurate even as flow path complexity increased. This is evident in data comparisons for the more complex yaw vectored three-hinge nozzle configurations. Upstream of sidewall trailing edges, two-dimensional inviscid flow solutions provided equally accurate predictions of two-dimensional nozzle pitch vectoring flow behavior. Moreover, the time involved in performing one of these solutions was much less than that required for an equivalent three-dimensional solution.

For a thrust reversing nozzle configuration, a two-dimensional inviscid flow solution provided marginal results. Navier-Stokes solutions are recommended for accurate performance evaluation, although Euler solutions may be valuable for understanding general flow behavior. Use of an unstructured flow solver allowed great time savings in grid generation about the complex thrust reverser, which featured multiple exit vanes and flow paths.

Acknowledgments

The information contained in this article represents the efforts of many. We thank Kevin Condon for accomplishing all conventional S/MTD nozzle two-dimensional analyses, and Robert Gillgrist for his contributions to every aspect of what has been presented. We also thank William Strang and David Amdahl for their patient and expert guidance in the use of each CFD tool discussed in this article. Finally, we thank Lewis Surber and Douglas Bowers for their overall guidance, advocacy, and exhaust nozzle integration expertise.

References

[1] "Exhaust Nozzles for Aerocontrol, Summary of Nozzle Static Test and Thrust Vectoring Utilization Results," WRDC-TR-89-3068, Vol. I, Wright-Patterson AFB, OH, July 1989.

[2] Emsley, H. T., "I3G/VIRGO, Interactive Graphics for Geometry Generation and Visual Interactive Rapid Grid Generation, User's Manual," WRDC-TM-90-317, Wright-Patterson AFB, OH, May 1990.

[3] Steinbrenner, J. P., Chawner, J. R., and Fouts, C. L., "A Structured Approach to Interactive Multiple Block Grid Generation," *AGARD Conference on Applications of Mesh Generation to Complex 3-D Confiqurations,* AGARD CP-464, March 1990.

[4] Holmes, D. G., and Snyder, D. D., "The Generation of Unstructured Triangular Meshes Using Delaunay Triangulation," *Numerical Grid Generation in Computational Fluid Mechanics '88,* edited by S. Sengupta et al., Pineridge, Swansea, Wales, UK, 1988, pp. 643–652.

[5] Jameson, A., et al., "Numerical Solutions of the Euler Equations by Finite Volume Methods Using Runge-Kutta Time-Stepping Schemes," AIAA Paper 81-1259, June 1981.

[6] Strang, W. Z., "Mercury User's Manual," Flight Dynamics Directorate, AFWAL-TM-88-217, Wright-Patterson AFB, OH, Nov. 1988.

[7] Lottati, I., Eidelman, S., and Drobot, A., "A Fast Unstructured Grid Second Order Godunov Solver (FUGGS)," AIAA Paper 90-0699, Jan. 1990.

[8] Collela, P., and Woodward, P. R., "The Piecewise Parabolic Method (PPM) for Gas-Dynamical Simulations," *Journal of Computational Physics,* Vol. 54, 1984, pp. 174–201.

[9] Moorhouse, D. J., et al., "Aerodynamic and Propulsive Control Development of the STOL and Maneuver Technology Demonstrator," *AGARD Conference on Aerodynamics of Combat Aircraft Controls and of Ground Effects,* AGARD CP-465, Oct. 1989.

[10] "STOL and Maneuver Technology Demonstrator (SMTD) Program, Nozzle Internal Aerodynamics Model Test Report," Pratt & Whitney, FR-18967, West Palm Beach, FL, Aug. 1985.

[11] Carson, G. T., and Capone, F. J., "Static Internal Performance of an Axisymmetric Nozzle with Multiaxis Thrust Vectoring Capability," proposed NASA TM.